Smart Materials and Structures

PAPER • **OPEN ACCESS**

On modeling the static shape control of an adaptive air foil bearing

To cite this article: Hossein Sadri *et al* 2020 *Smart Mater. Struct.* **29** 085043

View the article online for updates and enhancements.

This content was downloaded from IP address 47.68.67.61 on 05/08/2020 at 07:22

OPEN ACCESS
IOP Publishing
Smart Materials and Structures
Smart Mater. Struct. **29** (2020) 085043 (16pp)
https://doi.org/10.1088/1361-665X/ab99d7

On modeling the static shape control of an adaptive air foil bearing

Hossein Sadri[1], **Alexander Kyriazis**[1], **Henning Schlums**[1] and **Michael Sinapius**[1]

TU Braunschweig, Institut für Adaptronik und Funktionsintegration, Langer Kamp 6, D-38106 Braunschweig, Germany

E-mail: h.sadri@tu-braunschweig.de

Received 13 February 2020, revised 12 April 2020
Accepted for publication 5 June 2020
Published 16 July 2020

Abstract

Aerodynamic foil bearings are used in various industrial applications, e.g. in cooling turbines, small gas turbines or exhaust gas turbochargers, to support light, high-speed rotors under extreme operating conditions. Air (or another gas) is used as a lubricant in these bearings. In addition, the possible thermal deformations and production errors can be compensated by a flexible foil structure between the lubricant film and the bearing housing in air foil bearings. Since many static and dynamic properties of the lubricant are strongly dependent on the inner contour of the bearing, the idea of an adaptive air foil bearing (AAFB) is developed to optimize the performance of the bearing at different operating points. This paper focuses on a semi-analytical approach based on plate theory and the Ritz method for approximating the static shape control of a piezoelectrically actuatable AAFB. The main objective of this study is to consider adaptive bearing shells in calculating the behavior of an AAFB, as they provide additional degrees of freedom to a passive air foil bearing without adaptivity. Before the final step is taken, the model presented in this analysis is used for the shape optimization of the adaptive frame of AAFB in order to achieve the most efficient shape adaption with regard to target shapes.

Keywords: morphing, mfc, piezoelectric, active vibration control, shape control, air bearing, foil air bearing

(Some figures may appear in colour only in the online journal)

1. Introduction

Shape control can be considered as an effective solution to many problems, with the objective to change the geometrical properties of a specific structure. As a result of this fact, there are many fields of application especially in aerospace industry, where the performance of a system is optimized with regard to the operational conditions. This solution becomes significantly important in cases with fluid-solid interaction between different part of target design. As an example, a recent study by [1] investigates the design of a high-lift system for aircraft wings equipped with an adaptive droop nose. Both experimental and numerical investigations of this study show the need to optimize the adaptive mechanism as a function of structural stiffness and actuation in order to achieve the most effective advantages of the solution. Further discussions related to the smart morphing can be found in a recently published book [2]. Air foil bearings (AFB) are well suited for high-speed rotors and for operation at very high or low temperatures. Improving the load capacity, the lift-off speed and the stability limit are the most important challenges with regard to the development of air foil bearings. The application of adaptive strategies in the field of air foil bearing is described in a recent paper by Martowicz *et al* [3] to control the temperature gradient in AFBs. The authors show the effectiveness of the concept with integrated 36 thermoelectric

Original Content from this work may be used under the terms of the Creative Commons Attribution 4.0 licence. Any further distribution of this work must maintain attribution to the author(s) and the title of the work, journal citation and DOI.

modules on the basis of experimental results. On the other hand, many of the above design characteristics of air foil bearings are highly dependent on the shape of the bearing inner contour, which defines a large part of the lubricating film profile. The static and rotordynamic properties of air foil bearings with different profiles of the bearing inner contour are investigated in numerous studies (e.g. [4–6] and [7]). Such observations lead to different solutions for active bearing contour adjustment that benefit from various profiles of the lubricating film in a single bearing concept [8, 9, 10]. The concept proposed in [11], which is the focus of the present paper, differs clearly from the alternative concepts for adaptive bearings mentioned. In this case, internally contoured piezoelectrics in patch form are used to actuate the bearing inner contour in order to compromise between shape control and the required stiffness for operation. Figure 1.A and figure 1.B compare the classical air foil bearing of the bump-type with corresponding adaptive concept, in which an adaptable mechanism is used to actively manipulate the inner contour of the bearing. A classic foil bearing consists of a rigid housing and foil structure (bump-strip and top-foil). In an adaptive air foil bearing, the foil structure is supported by a flexible shell (or segment) and joints between the segment and the housing. On the outside of each supporting shell, there is a piezoelectric patch that generates the required mechanical strain in the circumferential direction of each pad to change the shape (radius and center of curvature) of the bearing clearance on demand.

This study extends the approach primarily investigated in [12] as a theoretical basis for the modeling and simulation of adaptive shells of the AAFB, which can be physically assumed as cylindrical sections of plates with different layers and materials. The static and dynamic behavior of cylindrical composite plates is the subject of a study done by Kassagne *et al* [13]. The laminate theory is used in this work in order to consider the properties of different layers and partly used stiffeners on cylindrical plates. The mathematical modeling of the static and dynamic response of piezoelectrically actuated (or sensed) beams and plates is the subject of many studies. Cheng *et al*[14] present an analytical model for the flat composite materials with piezoelectric layers for large deflections. The same authors [15] propose the Hermite differential quadrature as a numerical approach to solve the nonlinear differential equations that apply to the composites. Hadjigeorgiou *et al* [16] described shape control of straight beams using piezoelectric actuators. Koconis *et al* [17] presented a paper on shape control of composite plates with embedded actuators. They consider beams, plates and curved shells. The calculation is based on polynomial initial functions and the principle of minimum potential energy. Shivakumar and Ray [18] modelled flat plates with an integrated piezoelectric layer using harmonic initial functions for the entire plate. Agrawal *et al* [19] applied shape control to antenna reflectors. The reflector is modeled as a plate which is described by a finite element model. The achieved change in shape is compared to the desired shape. The square of the differences between both shapes yields an error function. The optimum actuator voltages are found minimizing the error function. Using the analytical transfer matrix formulation in combination with a technique to extend the small parameters in [20] it is demonstrated that neglecting the electromechanical coupling leads to significant errors in estimating the deformation of a three-layer actuator. A similar approach, extended for dynamic analysis, is presented in [21] to find modal solutions for the piezoelectric laminated plates with internal electrodes. This paper focuses

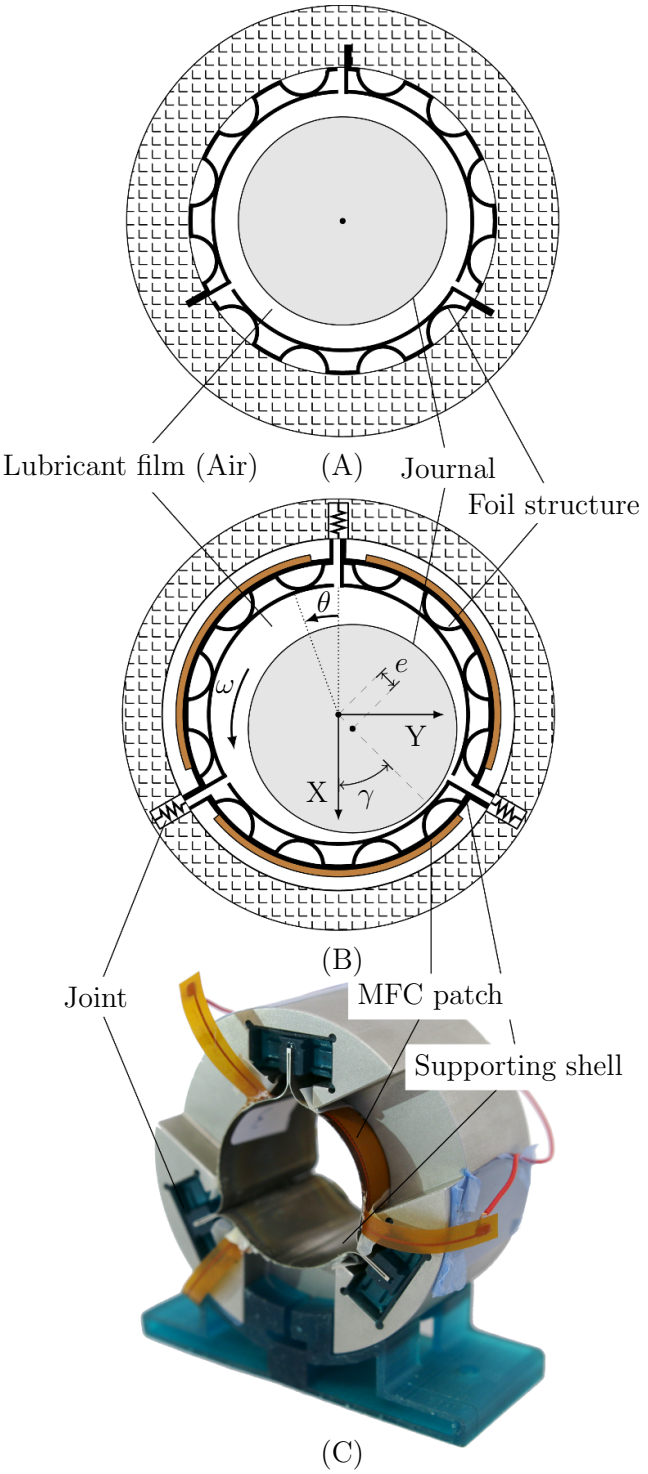

Figure 1. Schematic representation of (A) classical air foil bearing compared to (B) adaptive air foil bearing (AAFB) with corresponding coordinate system and (C) a functional model for AAFB.

on the modeling of the adaptive bearing segments (consisting of mechanical and piezoelectric materials) using the laminate theory (extendable for higher orders) and the Hamilton principle. The Ritz approach is used as a numerical basis for the approximation of the geometric changes due to actuation as well as external loads. To include the flexure joints between the bearing shells, a stiffness matrix is calculated from a finite element model. After verification, the model is used to perform parametric studies on the bearing shells, which form the basis for shape optimization.

2. Theoretical set-up for the model

There are two strong motivations to find an approach to describe the shape control of adaptive segments of an AAFB with a precise tool at low calculation cost. First, developing a numerical tool for the optimization of adaptive shells with respect to various parameters involved in both active and passive elements of the AAFB (e.g. type of actuators, thickness and material properties of the support shells, etc). Secondly, sufficient information on the behavior of adaptive shells under static and dynamic loads from the hydrodynamic pressure build-up by reaction forces of the foil structure seems to be necessary. Figure 1(C) shows a functional prototype for the actuation of AAFB (without mounting the foil structure) to be used as an adaptive interface for the shape morphing in adaptive air foil bearings. Three supporting shells with a thickness of 0.25 mm and a nominal diameter of 39.4 mm, which are manufactured as a one-piece frame made of stainless steel, are connected to the rigid housing by resin-printed bending joints. This allows sliding motion of each connection point between each pair of shells in a radial direction during actuation by the attached MFC (Piezoelectric Macrofiber Composite) without unwanted relative movement and backlash at adjacent points. Figure 2 shows a schematic representation of a single support shell and the local coordinate system to adjust the macro variables such as the deformation field and connect them to the micro effects such as strain terms and actuation in the piezoelectric patch. The following assumptions are considered for the representation of an equivalent model using the plate theory for static actuation in the mechanism:

(a) Each supporting shell is not completely covered with the bonded piezoelectric patch (consisting of two insulation layers and the piezoelectric fibers in between) in the circumferential direction. In contrast, the piezoelectric patch covers the shell in the axial direction.
(b) It is assumed that the adaptive shells of the functional model are manufactured symmetrically with respect to two perpendicular planes $\xi_2 - \xi_3$ and $\xi_1 - \xi_3$ (see figure 2)
(c) The displacements at the ends of the shells are small so that the flexure joints are replaced by corresponding linear elastic springs.
(d) The piezoelectric fibers (or elements), apart from the type (with d_{31} and d_{33} main effects), extend or contract over the length of the patches, resulting in a bending moment of the supporting shells.

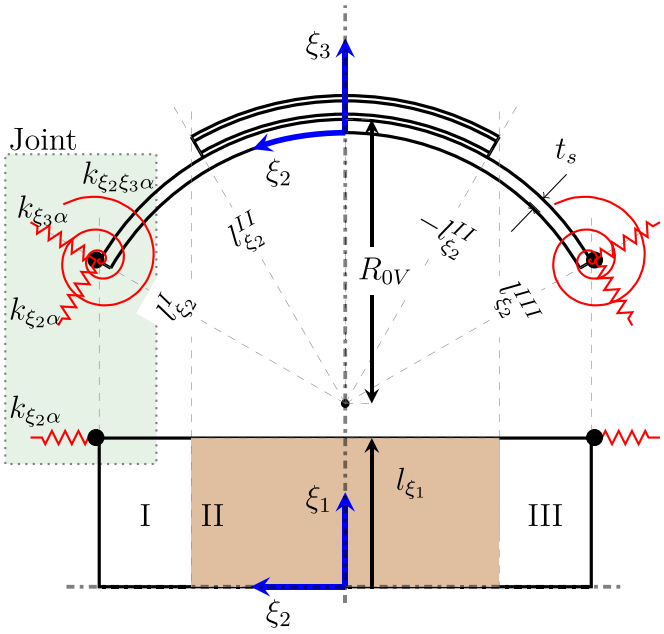

Figure 2. Coordinate system and discretization of a single segment of AAFB with elastic supports and MFC patch for actuation.

It should be noted that, despite the second assumption, the supporting shells may deform asymmetrically during the operation due to the non-uniform loading in the circumferential direction. Thus, in the next section, one half (relative to the axial coordinate) of each bearing segment is taken into account when creating the model.

2.1. Definition of stress-deformation relation

The mechanical stress can be related linearly to the electric field, with subsequent definition of inverse and direct piezoelectric effects in piezoelectric materials:

$$\{\sigma_p\} = [C_p]\{\epsilon_p\} - [e_p]^T\{E_p\} \tag{1}$$

$$\{D_p\} = [e_p]\{\epsilon_p\} + [\eta_p]\{E_p\} \tag{2}$$

where $\{D_p\}$ and $\{\sigma_p\}$ are vectors of electrical charge displacement and mechanical stress, $\{E_p\}$ and $\{\epsilon_p\}$ are electrical field strength and mechanical strain, $[e_p]$ is the matrix for the direct piezoelectric effect and $[\eta_p]$ and $[C_p]$ represent the dielectric constants and stiffness matrix. Due to the relationship in equation (2) the mechanical strain ε_p causes an electric displacement D_p by means of the direct piezoelectric effect, which is superimposed with the electric displacement due to the external electric field E_p. It should be mentioned that the equation introducing inverse piezoelectric effects from equation (1) can be presented with a different formulation as they are used in many studies in literature as follows:

$$\{\epsilon_p\} = [S_p]\{\sigma_p\} + [d_p]^T\{E_p\} \tag{3}$$

where $[S_p]$ and $[d_p]$ represent the matrices of compliance and piezoelectric strain constants. Seen the other way round, an external electric field generates a mechanical stress via the inverse piezoelectric effect, which is superimposed with the stress due to the mechanical strain in equation (1). The potential energy in the piezoelectric element consists of elongation and electrical terms as follows:

$$\Pi_p = \frac{1}{2}\int_{V_p}(\{\epsilon_p\}^T\{\sigma_p\} - \{D_p\}^T\{E_p\})dV_p = \frac{1}{2}\int_{V_p}(\{\epsilon_p\}^T[C_p]\{\epsilon_p\} - 2\{\epsilon_p\}^T[e_p]\{E_p\} - \{E_p\}^T[\eta_p]\{E_p\})dV_p \tag{4}$$

Considering zero matrices for dielectric and piezoelectric constants in non-piezoelectric layers, the linear strain-stress equation can be derived, as follows:

$$\{\sigma_{np}\} = [C_{np}]\{\epsilon_{np}\} \tag{5}$$

and the potential energy reduces to the single mechanical strain term:

$$\Pi_{np} = \frac{1}{2}\int_{V_{np}}\{\epsilon_{np}\}^T\{\sigma_{np}\}\,dV_{np} = \frac{1}{2}\int_{V_{np}}\{\epsilon_{np}\}^T[C_{np}]\{\epsilon_{np}\}\,dV_{np} \tag{6}$$

The supporting shells and the actuators, which are the focus of this work, are geometrically cutouts from thin-walled hollow cylinders. A description in cylinder coordinates is therefore recommended. In this sense, a geometric description of adaptive shells in cylindrical coordinates is used. The strain-displacement (Karman strain) in an orthogonal curvilinear coordinate system can be expressed as follows [22]:

$$\begin{aligned}
\epsilon_{\xi_1} &= \frac{\partial u_{\xi_1}}{\partial \xi_1} + \frac{1}{2}\left(\frac{\partial u_{\xi_3}}{\partial \xi_1}\right)^2 + \xi_3\frac{\partial \psi_{\xi_1}}{\partial \xi_1}\\
\epsilon_{\xi_2} &= \frac{\partial u_{\xi_2}}{\partial \xi_2} + \epsilon_{\xi_2,circ} + \frac{1}{2}\left(\frac{\partial u_{\xi_3}}{\partial \xi_2}\right)^2 + \xi_3\frac{\partial \psi_{\xi_2}}{\partial \xi_2}\\
\gamma_{\xi_1\xi_2} &= \frac{\partial u_{\xi_1}}{\partial \xi_2} + \frac{\partial u_{\xi_2}}{\partial \xi_1} + \frac{\partial u_{\xi_3}}{\partial \xi_1}\frac{\partial u_{\xi_3}}{\partial \xi_2} + \xi_3\left(\frac{\partial \psi_{\xi_1}}{\partial \xi_2} + \frac{\partial \psi_{\xi_2}}{\partial \xi_1}\right)\\
\gamma_{\xi_1\xi_3} &= K_{\xi_1}\left(\frac{\partial u_{\xi_3}}{\partial \xi_1} + \psi_{\xi_1}\right)\\
\gamma_{\xi_2\xi_3} &= K_{\xi_2}\left(\frac{\partial u_{\xi_3}}{\partial \xi_2} + \psi_{\xi_2}\right)
\end{aligned} \tag{7}$$

Here u_{ξ_1,ξ_2,ξ_3} and ψ_{ξ_1,ξ_2} represent the global displacements and rotations with respect to the assumed coordinate system. Moreover, K_{ξ_1} and K_{ξ_2} are shear correction factors. Due to the large ratio between the length and thickness of different components of the adaptive shells, the normal strain in radial direction is neglected, thus:

$$\epsilon_{\xi_3} = \frac{\partial u_{\xi_3}}{\partial \xi_3} = 0 \tag{8}$$

Moreover, the circumferential strain in second term of equation (7), $\epsilon_{\xi_2,circ}$, results from the uniform radial expansion in a cylindrical shell:

$$\epsilon_{\xi_2,circ} = \frac{(R_c + u_{\xi_3}) - R_c}{R_c} = \frac{u_{\xi_3}}{R_c}$$

with:

$$R_c = R_{0\,\mathrm{v}} - t_s + \xi_3 \tag{9}$$

The general time-independent displacements at a generic point of each piezoelectric and non-piezoelectric layer in the cylindrical reference coordinate system (ξ_1, ξ_2, ξ_3) with respect to Mindlin–Reissner theory of plates are given by:

$$\{U(\xi_1,\xi_2,\xi_3)\} = \begin{Bmatrix} u_{\xi_1}(\xi_1,\xi_2) + \xi_3\psi_{\xi_1}(\xi_1,\xi_2) \\ u_{\xi_2}(\xi_1,\xi_2)\left(\frac{R_c}{R_{0\,\mathrm{v}} - t_s}\right) + \xi_3\psi_{\xi_2}(\xi_1,\xi_2) \\ u_{\xi_3}(\xi_1,\xi_2) \end{Bmatrix} \tag{10}$$

The displacement field in equation (10) cannot be used for the solution of many problems in complicated structures, because the differential equations of motion cannot be solved analytically in these cases. Therefore, an approximate description of the displacement field depending on the physics and the type of the desired solution for a certain field of application is demanded.

3. Ritz method and approximated displacement field

The Ritz method is a widely used approach for the approximated solution of a given differential equation in which an exact solution is not or hardly achieved. For the application of the Ritz method, the mathematical problem must be present in a so-called variation formulation. The Ritz method is based on approximating the solution with a sum of basic functions. The functions mentioned in the model have a special role, therefore they are separated from the local deformation approach in equation (10). The previously explained formulation of the displacement field are general analytics. In accordance with this, the basic functions defined for the Ritz approach, like many other weighted residual methods, can perfectly describe the state of a system for a certain range of initial and boundary value problems, if chosen properly. The approximated displacement field can be defined in the following general form:

$$\begin{aligned}
u_{\xi_1} &= \sum_{m=0}^{\infty}\sum_{n=0}^{\infty}\hat{U}_{\xi_1}^{mn} f_1^{mn}(\xi_1,\xi_2)\\
u_{\xi_2} &= \sum_{m=0}^{\infty}\sum_{n=0}^{\infty}\hat{U}_{\xi_2}^{mn} f_2^{mn}(\xi_1,\xi_2)\\
u_{\xi_3} &= \sum_{m=0}^{\infty}\sum_{n=0}^{\infty}\hat{U}_{\xi_3}^{mn} f_3^{mn}(\xi_1,\xi_2)\\
\psi_{\xi_1} &= \sum_{m=0}^{\infty}\sum_{n=0}^{\infty}\hat{\Psi}_{\xi_1}^{mn} f_1^{mn}(\xi_1,\xi_2)
\end{aligned}$$

$$\psi_{\xi_2} = \sum_{m=0}^{\infty}\sum_{n=0}^{\infty} \hat{\Psi}_{\xi_2}^{mn} f_2^{mn}(\xi_1,\xi_2) \tag{11}$$

Here $\hat{U}_{\xi_1}^{mn}$, $\hat{U}_{\xi_2}^{mn}$, $\hat{U}_{\xi_3}^{mn}$, $\hat{\Psi}_{\xi_1}^{mn}$ and $\hat{\Psi}_{\xi_2}^{mn}$ are unknowns representing the weighting factor of each basic function. These weighting factors are multiplied by their corresponding basic functions and summed up to define the approximate solution for the displacement field. It should be noted that the basic functions are so-called permitted functions. These fulfill the essential or geometrical boundary conditions, e.g. no curvature occures at the free edges and are χ times continuously differentiable, if 2χ represents the order of the considered differential equation with regard to the variables [23] (in this case: ξ_1 and ξ_2). This is the case if the solution function is an extremum of a function [24], e.g. when solving beam and plate models, where the final solution describes the deformation of the mechanical component. In a static model it is assumed that the beam or plate is massless and reacts immediately to external forces with a deformation without transient oscillation. As a result of this assumption, the kinetic energy is zero. Therefore, only potential energy and the work of external forces on the system are considered. In mechanical systems, this variation formulation directly follows the Hamilton principle, which can be expressed in the following form for static models:

$$\frac{\partial L}{\partial \vec{q}} = \{0\} \tag{12}$$

where the Lagrangian L consists of the potential energy in the system and the work of external forces:

$$L(\vec{q}) = W_{ex}(\vec{q}) - \Pi_{np,p}(\vec{q}) \tag{13}$$

If the Ritz approach for the displacement field is used in equation (12), an expression is obtained for the action depending on the parameters $\hat{U}_{\xi_1}^{mn},\ldots,\hat{\Psi}_{\xi_2}^{mn}$. To minimize the left hand side of the equation (12), after this substitution no variation (i.e. gateaux derivation) needs to be performed. It is now sufficient to differentiate the action function according to the parameters $\hat{U}_{\xi_1}^{mn},\ldots,\hat{\Psi}_{\xi_2}^{mn}$ and to determine the steady-state point. This condition provides a system of equations with nth equations for the nth unknowns. The approximated solution in equation (11) presents itself as the linear combination of the basic functions, which has the smallest action of all possible linear combinations of the basic functions. Related to the basic functions, it is therefore the best possible approximation of the true solution. The variation problem can now be solved by solving an algebraic system of equations. For the solution of such algebraic systems of equations efficient algorithms, such as the Newton method, are to be used.

As already mentioned, it is assumed that the adaptive shells (in non-loaded state) have two symmetry planes, namely the $\xi_1-\xi_3$ plane and the $\xi_2-\xi_3$ plane. The adaptive shells can, however, deform asymmetrically during operation, since the shells are externally loaded by asymmetrical reaction forces of the foil structure caused by an eccentric position of the journal. As a result, the following conditions must be applied in the basic functions so that the remaining symmetry plane $\xi_1-\xi_3$ can be correctly considered:

$$\begin{aligned}
u_{\xi_1}(\xi_1,\xi_2) &= -u_{\xi_1}(-\xi_1,\xi_2)\\
u_{\xi_2}(\xi_1,\xi_2) &= u_{\xi_2}(-\xi_1,\xi_2)\\
u_{\xi_3}(\xi_1,\xi_2) &= u_{\xi_3}(-\xi_1,\xi_2)\\
\psi_{\xi_1}(\xi_1,\xi_2) &= -\psi_{\xi_1}(-\xi_1,\xi_2)\\
\psi_{\xi_2}(\xi_1,\xi_2) &= \psi_{\xi_2}(-\xi_1,\xi_2)
\end{aligned} \tag{14}$$

Assuming a single bearing shell in different main parts, it can be seen that there are changes in stiffness at the borders of each section. In addition, actuation with the corresponding piezoelectric patches is only possible in the section II. Now the approximation functions for both areas are set up separately and linked with consistency conditions between any two different sections of the bearing shell:

$$\begin{aligned}
u_{\xi_1}^{I}(\xi_1,l_{\xi_2}^{II}) &= u_{\xi_1}^{II}(\xi_1,l_{\xi_2}^{II})\\
u_{\xi_2}^{I}(\xi_1,l_{\xi_2}^{II}) &= u_{\xi_2}^{II}(\xi_1,l_{\xi_2}^{II})\\
u_{\xi_3}^{I}(\xi_1,l_{\xi_2}^{II}) &= u_{\xi_3}^{II}(\xi_1,l_{\xi_2}^{II})\\
\psi_{\xi_1}^{I}(\xi_1,l_{\xi_2}^{II}) &= \psi_{\xi_1}^{II}(\xi_1,l_{\xi_2}^{II})\\
\psi_{\xi_2}^{I}(\xi_1,l_{\xi_2}^{II}) &= \psi_{\xi_2}^{II}(\xi_1,l_{\xi_2}^{II})
\end{aligned} \tag{15}$$

Similar conditions have to be considered for the boundary between area II and III at $\xi_2 = -l_{\xi_2}^{II}$. The consistency conditions must be fulfilled by the displacement functions. For this purpose, these conditions are established and appended to the expression for energy and external work using Lagrangian multipliers. The minimization of the general energy thus becomes a minimization under secondary conditions. In addition to the coefficients of the basic functions, the resulting energy expression must also be differentiated by the Lagrange multipliers $l_1\ldots l_{10}$ when searching for the energy minimum, as follows:

$$\frac{\partial L'}{\partial \vec{q}} = \{0\} \tag{16}$$

where:

$$L' = L(\vec{q}) + l_1 f_{u_{\xi_1}}^{I,II} + \cdots + l_5 f_{\psi_{\xi_2}}^{I,II} + l_6 f_{u_{\xi_1}}^{II,III} + \cdots + l_{10} f_{\psi_{\xi_2}}^{II,III}. \tag{17}$$

Here $f_{u_{\xi_1}}^{I,II}, f_{u_{\xi_2}}^{I,II}\ldots f_{\psi_{\xi_2}}^{I,II}$ (and the same for the consistency between area II and III) represent the conditions in equation (14) in a reformed formulation as $f=0$. Both polynomials and harmonic functions are suitable as basic functions for AAFB's adaptive shells. However, harmonic functions usually work with less unknowns and, on the contrary, it is easier to meet the consistency conditions at the boundaries of different parts of the adaptive shell using polynomials. Considerations of this kind lead to the definition of a hybrid approach, in which the deformation in ξ_2-direction is to be determined by polynomial basic functions and the deformation in ξ_1-direction by harmonic basic functions:

$$f_1^{mn}(\xi_1,\xi_2) = \xi_2^n \sin\alpha_m\xi_1$$

$$f_2^{mn}(\xi_1,\xi_2) = \xi_2^n \cos\alpha_m\xi_1$$
$$f_3^{mn}(\xi_1,\xi_2) = \xi_2^n \cos\alpha_m\xi_1$$
$$\text{with }:\alpha_m = \frac{m\pi}{l_{\xi_1}} \tag{18}$$

where m and nth can be considered as the number of different combinations of solutions in equation (11) in axial and circumferential directions weighted with corresponding unknown constants. It should be noted that the number of solution functions in the circumferential direction is also the order of the polynomial assumed for the hybrid solution. The formulation of the solution in the form considered by weighted residual methods has the advantage that only a small number of approximation functions can suffice for a good approximation quality in order to be able to gain first statements about the system behavior [23]. Otherwise, it is usually sufficient to increase the number of basic functions for the approximated solution in order to achieve the desired solution close to the exact solution, if the basic functions are mathematically correct but physically not meaningful [23].

4. Influence of elastic boundary conditions

The energy stored in the elastic suspension can be considered as potential energy and should be added to the terms of energy in piezoelectric and non-piezoelectric elements in the single supporting shell. Back to the schematic representation of a single support shell in the functional model, the solid joints react to forces in the circumferential direction of the bearing shells as well as to forces in the radial direction or to acting moments. So the bending joints at two ends of each shell can be simplified with three linear springs, namely in ξ_3 direction, perpendicular to ξ_3 and around the ξ_1 axis, which reacts to the forces and in different directions the single corresponding moment (represented by α in figure 2). In the case of the functional model under investigation, the flexure joints are connected to the shell at both ends via a single connection point. Based on this and on the basis of the linear elastic assumption for flexure joints, the potential energy of each joint can be represented in simplified form as follows:

$$\Pi^J = \frac{1}{2}\{U_J\}^T[C_J]\{U_J\} \tag{19}$$

where $\{U^J\}$ is the displacement vector at the end of a single shell (where the joints are connected). Furthermore, it should be generally assumed that, a force in one of these three directions in a solid joint does not only cause a deformation in the same direction, but also a tilting of the joint and possibly also a deformation in other directions. Consequently, the stiffness matrix $[C^J]$ is not necessarily a diagonal one. There are inherently some further assumptions in the stiffnesses determined here. The omission of the consideration of stiffnesses in axial direction of the bearing shells is synonymous with the assumption that there is no potential energy in the deformation of the bearing shells in axial direction. This can be achieved either by zero stiffness or by locking the corresponding degree of freedom. It is assumed that the second case is a better representation of reality. Accordingly, further boundary conditions must be introduced for the bearing shell at the supporting points, which are formulated below. It should be mentioned that, $l_{\xi_2}^{I,III}$ is the angle at which the bearing shell connects to the elastic support:

$$u_{\xi_1}(\xi_1, l_{\xi_2}^{I,III}), \psi_{\xi_1}(\xi_1, l_{\xi_2}^{I,III}) = 0 \tag{20}$$

The determination of the stiffness matrix must be carried out individually for each different type of joint. The elastic suspension and the local coordinate system on the right and left side are shown in figure 3. In order to determine the compliance of the flexure joints, forces in the radial direction and in the circumferential direction are applied to the connection points for the bearing shells in the FEM simulation (ANSYS Workbench 18.1). In addition, the connection points are loaded with a torque to individually observe the tilt angle of the leading edge of the joint. It should be noted that the angle α represents the same angle of inclination as the ends of the bearing shell, since it is assumed that the support shells are completely connected to the joints at the end points without any slip effect. The compliance matrix is calculated in the first step using deformations extracted from FEM model. This matrix is the inverted stiffness matrix, which relates the deformation terms of the allowed degrees of freedom to the vector consisting force terms and torque acting on mentioned DOFs, as it follows:

$$\{U^J\} = \begin{pmatrix} u_{\xi_2}^R(\xi_1, l_{\xi_2}^{I,III}) \\ u_{\xi_3}^R(\xi_1, l_{\xi_2}^{I,III}) \\ \psi_{\xi_2}^R(\xi_1, l_{\xi_2}^{I,III}) \\ u_{\xi_2}^L(\xi_1, l_{\xi_2}^{I,III}) \\ u_{\xi_3}^L(\xi_1, l_{\xi_2}^{I,III}) \\ \psi_{\xi_2}^L(\xi_1, l_{\xi_2}^{I,III}) \end{pmatrix} = (S_J)_{6\times6} \times \begin{pmatrix} F_{\xi_2}^R \\ F_{\xi_3}^R \\ M_{\xi_2}^R \\ F_{\xi_2}^L \\ F_{\xi_3}^L \\ M_{\xi_2}^L \end{pmatrix} \tag{21}$$

where $[S^J]$ is the compliance matrix of the flexure joint (containing direct and coupled terms), $F_{\xi_2}^{R,L}$ and $F_{\xi_3}^{R,L}$ are tangential and radial forces and $M_{\xi_2}^{R,L}$ torques acting respectively on the right and left sides of the joint. Since the forces must be specified component by component in the global Cartesian coordinate system, the angle ϕ shown in figure 3 is required to calculate the individual force components. Two 10 N force vectors in radial and tangential directions of the joint ($F_{\xi_2}^{R,L} = F_{\xi_3}^{R,L} = 10$ N) end and a 10 Nmm torque ($M_{\xi_2}^{R,L} = 10$ N.mm) around axial direction are applied in the model. To determine the compliance matrix, the resulting deformation must first be calculated for the individual loads. Since this deformation is specified in the global coordinate system, it must first be transformed into the local coordinate system. The angle change α is calculated using the analytical geometry and a reference edge. The principle is shown in figure 3 The figure shows the enlarged connection point for a bearing shell. The angle of rotation can be calculated from the angle between the two vectors $\vec{a}_1$ and $\vec{a}_2$. The vector $\vec{a}_1$ is the distance vector between the two considered edge points A and C before the deformation.

The vector $\vec{a}_2$ denotes the distance between the edge points B and D in the deformed state. The following equation applies to the angle:

$$\alpha = \psi^{R}_{\xi_2}(\xi_1, l^{I,III}_{\xi_2}) = acos(\frac{\vec{a_1}.\vec{a_2}}{|a_1|.|a_2|}) \tag{22}$$

The tilt angle on the left hand side of the joint can be achieved in the same way. After defining the terms of the joint displacement matrix, the compliance matrix can be calculated from equation (21). The calculated compliance matrix is almost symmetrical, but numerical deviations cause a slight asymmetry. Hence, before inversion into the stiffness matrix, the compliance matrix is symmetrized by the summation of original compliance matrix and it is transposed matrix: $2[S_J]_{new} = [S_J] + [S_J]^T$. When calculating the matrix, the units have to be considered very carefully. Different entries in the matrix have different units and must therefore be multiplied by other factors when converting to SI base units. Inverting the compliance matrix results in the stiffness matrix $[C_J]$, as it follows:

$$[C_J] = 10^3 \times \tag{23}$$

$$\begin{pmatrix} 0.6130\frac{N}{m} & -0.5192\frac{N}{m} & -0.7542\,\text{N} & -0.3288\frac{N}{m} & 0.4996\frac{N}{m} & 1.0451\,\text{N} \\ -0.5192\frac{N}{m} & 0.7639\frac{N}{m} & 1.5978\,\text{N} & 0.4996\frac{N}{m} & -0.6587\frac{N}{m} & -1.3155\,\text{N} \\ -0.7542\,\text{N} & 1.5978\,\text{N} & 4.2740\,\text{N}.m & 1.0451\,\text{N} & -2.3155\,\text{N} & -2.5795\,\text{N}.m \\ -0.3288\frac{N}{m} & 0.4996\frac{N}{m} & 1.0451\,\text{N} & 0.6130\frac{N}{m} & -0.5192\frac{N}{m} & -0.7542\,\text{N} \\ 0.4996\frac{N}{m} & -0.6587\frac{N}{m} & -1.3155\,\text{N} & -0.5192\frac{N}{m} & 0.7639\frac{N}{m} & 1.5978\,\text{N} \\ 1.0451\,\text{N} & -1.3155\,\text{N} & -2.5795\,\text{N}.m & -0.7542\,\text{N} & 1.5978\,\text{N} & 4.2740\,\text{N}.m \end{pmatrix} \tag{24}$$

As assumed, coupling stiffnesses occur that combine a deflection in each direction with a force in another. Looking at the joints as external work generators (or as absorbers for the energy derived from bearing shells), the Maxwell-Betti law of reciprocal deflections is fulfilled in terms of both the compliance and the stiffness matrix. In other words, the work that is defined by a force acting on an individual degree of freedom of the joint (e.g. the ξ_2-direction) and the deflection caused in another (e.g. the ξ_3-direction) corresponds to the work performed in reverse direction.

5. Results and discussion

The main objective of an AAFB is to benefit from different bore contours in a single bearing and actively modify the shape. For the AAFB, two target shapes are generally considered, each offering corresponding advantages for various operating conditions, namely the circular and non-circular contour. In the tribology of AFBs, the non-circular bore shape is usually referred to as the preloaded configuration due to the hydrodynamic preloading effects of the lubricating film within this configuration. The radius of the bearing inner contour with preloaded shape (based on the classical preload model [7] [5]) can be mathematically described as follows:

$$R_{BCS}(\theta) = r + c_0 - r_p \cos(\theta - \theta_p) \tag{25}$$

where r is the radius of journal, c_0 and r_p are nominal clearance and preload factor of the bearing and θ_p is called pivot angle. The AAFB both in circular and preloaded configurations is shown in figure 4 assuming a constant length of each supporting shell in circumferential direction. The model presented in previous sections is used for the motivations, which are explained in the introduction. The deliberate structure of the model for discussing the results in the next sections is shown in figure 5. The functional model is assumed to be a system consisting of three supporting shells and three elastic supports between each pair. A single bearing shell is discretized into three sections, namely two parts, the two ends of the shells exposed with piezoelectric patches (Sections I and III) and a part in between completely covered by the actuator (section II). The considered material properties of the actuators and the shell are listed in table 1. The calculated stiffness matrix of the flexure joints in previous section is used to couple the discussed degrees of freedom of ending parts (sections I and III) of the adjacent shells. The terms of potential energy for each part of each shell of equations (4) and (6) and flexure joints of equation (19) are coded, related to strain terms of equation (7) and displacement fields described by the Ritz method. The adhesive layer between actuator and shell is assumed to be ideally thin and stiff. Furthermore, the use of first order shear deformations with independent terms (ψ_{ξ_1} and ψ_{ξ_2}) in equation (10) has no significant effect on the radius change of the bearing shells with investigated dimensions, as already observed in [12]. As a result, the simulations performed for this paper are limited to the Kirchhof Plate Theory ($\psi_{\xi_1} = \partial u_{\xi_3}/\partial\xi_1$ and $\psi_{\xi_2} = \partial u_{\xi_3}/\partial\xi_2$) for reasons of calculation time efficiency. The terms for potential energy and consistency conditions of equation (15) (all consisting of unknown vectors describing the displacement fields) are added to the Lagrangian in equation (17). Finally, the change of the total energy of the system (right hand side of equation (13)) with the use of Newton method is considered to be as close to zero as possible, which leads to the numerical definition of the unknown vector and thus to the displacement with regard to the local coordinate system of each shell. Local deformations are later recalculated in the global coordinate system of the bearing.

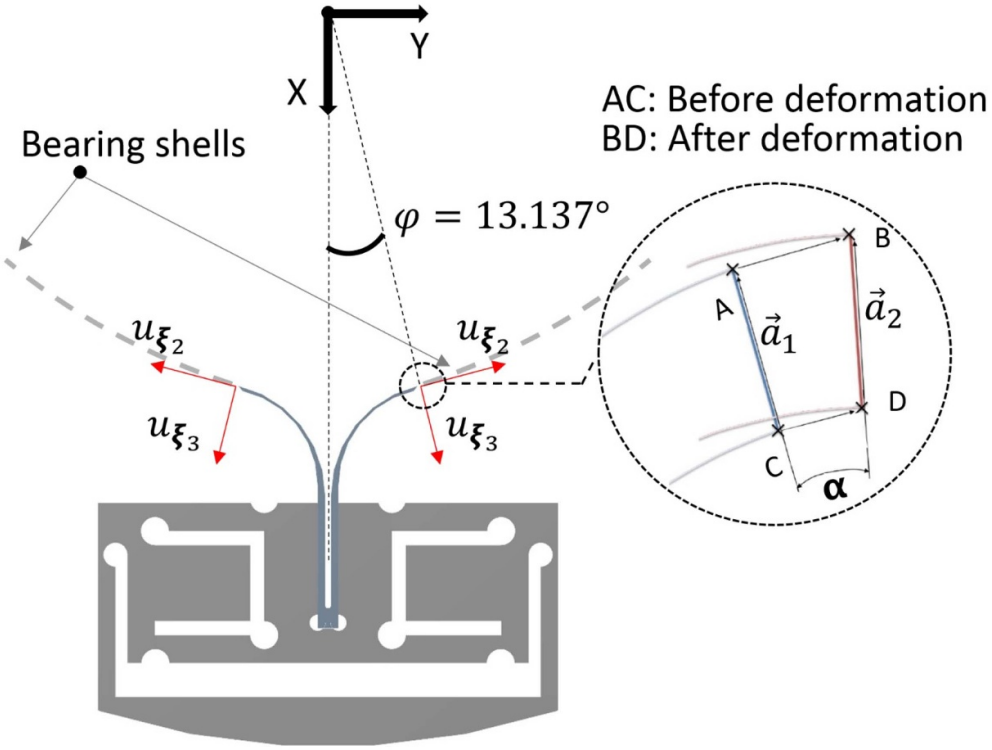

Figure 3. The flexure joint of the functional model.

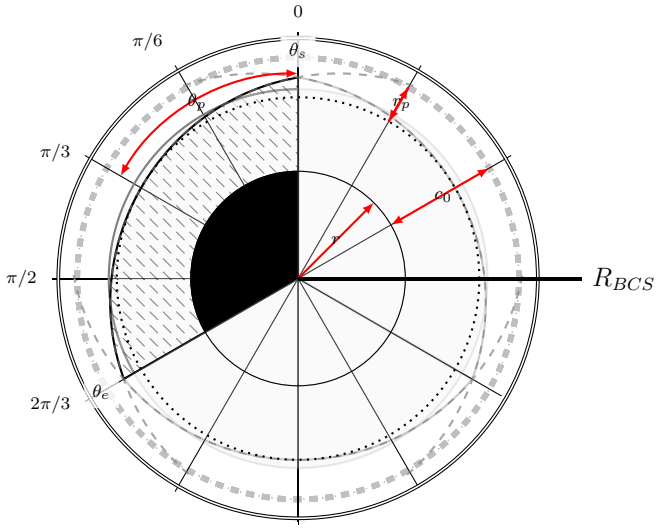

Figure 4. Bearing polar coordinate system and the definition of actual clearance of an AAFB with a non-circular configuration based on the classical preload model compared to the target circular shape.

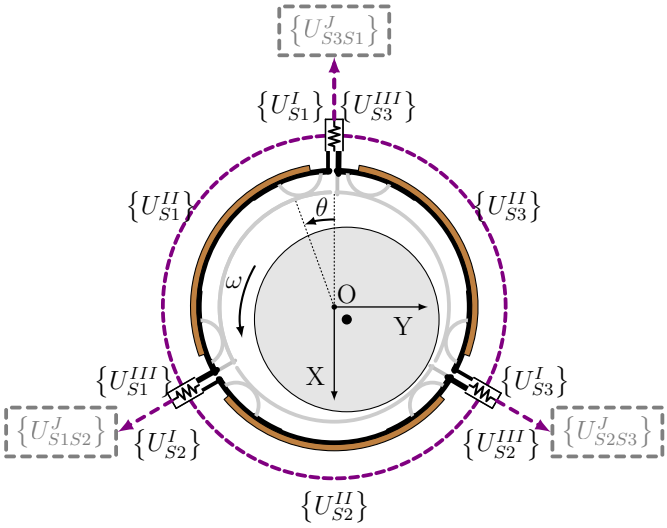

Figure 5. Set-up of the model for the investigated AAFB in a three-pad configuration.

Figure 6 shows the result of a convergence study carried out on the hybrid solution shown in equation (18) with respect to the order of the polynomial part by showing the absolute radius change of the supporting shells of the functional model (in relation to the local coordinate system of the shell) as a function of the actuation voltage. In this case two first modes in axial direction (m = 0 : 1) and up to six first modes in circumferential direction (n = 0 : 5) are considered for the consideration of displacement fields. As can be seen, the cubic polynomials can be used for further investigations, since third-degree polynomials provide a satisfactory reliability for the whole range of applicable voltage with a very low computational effort compared to the higher degrees. In the next step, figure 7 shows the change of the shell radius under consideration and neglect of non-linear strain terms in equation (7).

Table 1. Material properties of supporting shell, MFC-actuator used in the functional model investigated in this study.

Parameter	Value
Young's modulus (shell)	193 [GPa]
Poissons ratio (shell)	0.31 [−]
Initial thickness (shell)	0.25 [mm]
Initial radius (shell)	20.641 [mm]
Width (shell)	40 [mm]
Young's modulus (actuator), E_1	18 [GPa]
Young's modulus (actuator), E_2	15.9 [GPa]
Young's modulus (actuator), E_3	13.5 [GPa]
Shear modulus (actuator), G_{12}	9 [GPa]
Shear modulus (actuator), G_{31}	6.75 [GPa]
Shear modulus (actuator), G_{23}	5.515 [GPa]
Poissons ratio (actuator), ν_{12}	0.31 [−]
Poissons ratio (actuator), ν_{31}	0.31 [−]
Poissons ratio (actuator), ν_{32}	0.31 [−]
Initial thickness (actuator)	0.3 [mm]
Width (actuator)	40 [mm]
d_{33}[25]	400 $[\frac{pC}{N}]$

Based on this, no significant deviation of the geometric properties of the investigated functional model can be observed. At the end of applied voltage range there is a detected influence of non-linear terms which can be interpreted as a dedication of the applied energy to the non-linear terms (quadratic deformation in radial direction with respect to circumferential and axial coordinates) and thus a reduction of the radius change in general. Accordingly, the non-linear terms are disregarded in the further analysis of this study in order to save calculation time. Furthermore, figure 7 also shows the radius change from experimental efforts in [11] resulting from periodic measurements when actuating the actuators with a 2 Hz input signal. The applicable radius change of the bearing shells simulated in this section shows a good agreement with the experimental results. However, the slightly non-linear behavior observed in practical tests may be due to non-linearity in joints or the hysteresis effect in piezoelectric actuators, which requires further investigation. The change of radius with respect to the bearing global coordinate system for different actuator input signals (and no external loading of the mechanism) is shown in the polar coordinate system of the bearing in figure 8. In addition, the same results are shown in figure 9 for the three target shapes of AAFB ($r = 18.9$ mm) from [11] to compare them with the simulated results of the functional model for different actuation voltages. Starting from the slightly non-circular geometry, actuating the piezoelectric patches with the maximum negative voltage leads to a deformation of the bearing shells that corresponds in good approximation to the strongly non-circular geometry. However, actuating the mechanism with the maximum applicable voltage results in an over-circular shape where the radius of each shell is smaller than that of the circular target shape ($r_p < 0$). In order to better understand how the adaptive interface is able to adapt an actual shape close to the target shapes and possibly improve the shape adaptation, an optimization procedure is discussed in the next section. The result can be a roadmap to better understand the circumstances, under which the shape control strategy for an AAFB can be perfectly implemented.

5.1. Shape optimization

5.1.1. Influencing parameters. As can be seen in the previous work [12], the modulus of elasticity of the shell material and the geometric parameter of the supporting shells can influence the solution shape control in an AAFB. In addition to the bearing shells, the mechanical stiffness (and damping) properties of the joints can influence the amount of energy consumed to generate the required strain for the nominal shape control. These parameters determine the global stiffness ratio between actuator and bearing shell and thus also the deformation achievable during actuation. The shape optimization in this study refers to the adaptation of influencing variables to perform the shape change from an actual shape as close as possible to the intended shape. The main focus of the shape optimization study in this section is on the properties of the support shells. If the deformation is intended to adopt a certain shape into which the bearing shell is to be placed, a local variation of the stiffness ratio can be regarded as an option in addition to the global variation of the stiffness ratio. Since the material properties cannot be varied locally, a local variation of the shell thickness is to be used to adjust the stiffness ratio. In line with this, the shell thickness is assumed to be variable with respect to the circumferential coordinate ξ_2. As a measure to describe this variation, a parameter called convexity κ is introduced, which describes the thickness variation. A shell that is thicker in the center than in the elastic support area is called a convex shell. Conversely, a shell that is thicker in the elastic support area than in the center is called a concave shell or a negative convex shell. The thickness variation with the coordinate ξ_2 is described by the following equation:

$$t_s(\xi_2) = t_0 \cdot \left(1 + \kappa \cdot \left(1 - \frac{\xi_2^2}{(l^I_{\xi_2})^2}\right)\right) \tag{26}$$

The equation shows that a convexity of $\kappa = 0$ results in a bearing shell with a constant thickness $t_s(\xi_2) = t_0$. A convexity of $\kappa = 1$ means that the bearing shell in the middle ($\xi_2 = 0$) is twice as thick as in the suspension ($\xi_2 = l^I_{\xi_2}$ and $\xi_2 = l^{III}_{\xi_2}$). A convexity of $\kappa = -1$ would mean that the bearing shell achieves a thickness of $t_s(\xi_2 = 0) = 0$ in the middle. This does not make sense, since the bearing shell would then disintegrate into two parts without an applied piezo actuator, so the convexity cannot reach the lower limit of $\kappa = -1$. However, there are no upper limits to the convexity. A single bearing shell with different values of convexity is shown in figure 10.

5.1.2. Definition of deviation and optimization algorithm:. The goal of shape optimization is to achieve a deformation during actuation that corresponds as closely as possible to a given target deformation. The specified target deformation is determined by the following function:

$$w_{\text{target}}(\theta) = R^{\text{BCS}}_{\text{target}}(\theta) - R^{\text{BCS}}_0(\theta) \tag{27}$$

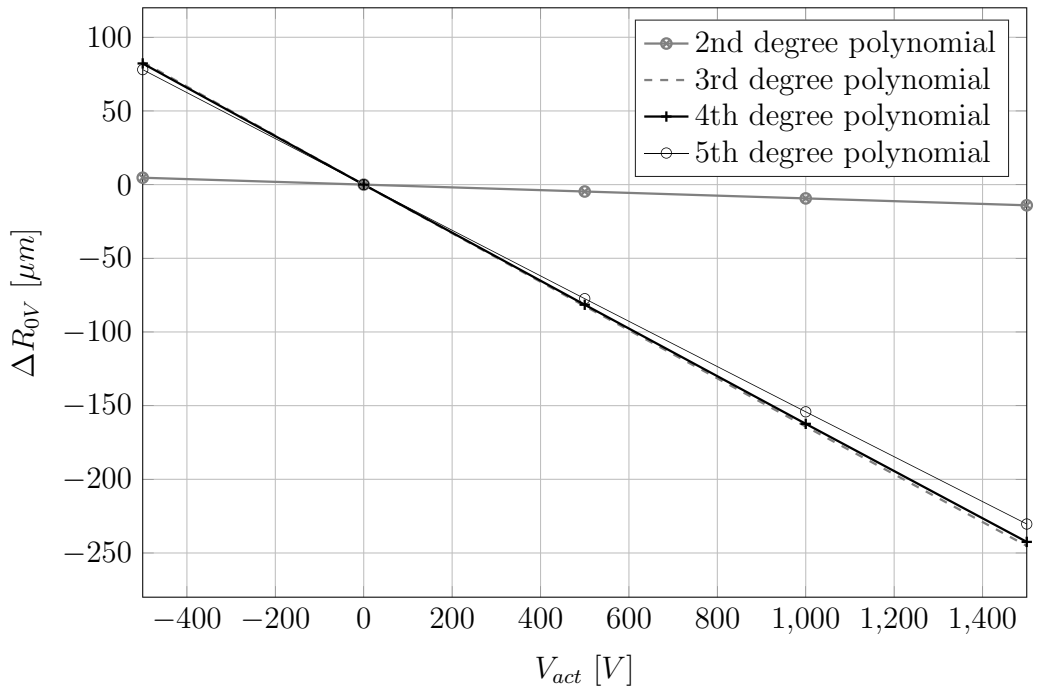

Figure 6. Convergence study on the polynomial part of hybrid solution function.

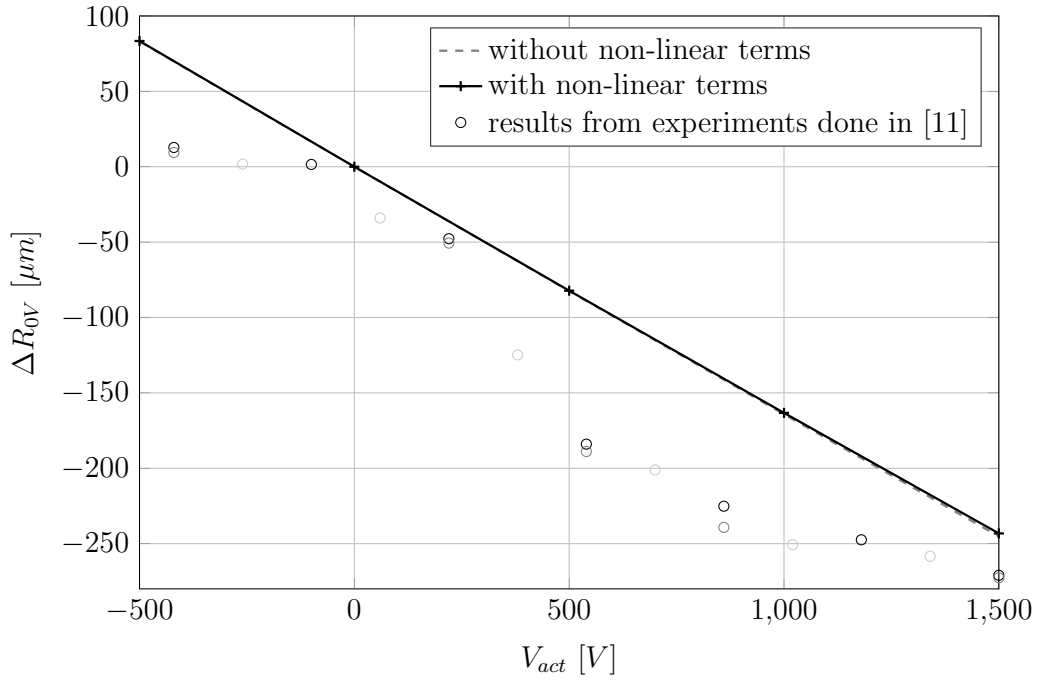

Figure 7. Radius change of a single supporting shell in unloaded state as a function of actuation voltage, with and without considering the non-linear terms in equation (7)

Here $R_{\text{target}}^{\text{BCS}}$ and R_0^{BCS} represent the desired (each one of previously investigated configurations in [11]) and initial profile function with respect to the bearing coordinate system. On the other hand, a similar function must be presented to quantify the difference between the initial and actual shape of the bearing shells for each operating voltage in terms of optimization variables (thickness and convexity):

$$w_{is}(\theta) = R_{\text{act}}^{\text{BCS}}(\theta, V_{\text{act}}, \kappa, t_0) - R_0^{\text{BCS}}(\theta) \tag{28}$$

Here $R_{\text{act}}^{\text{BCS}}$ specifies the actuated profile of the bearing shells for each optimization variable related to the bearing coordinate system. Before performing the optimization, a

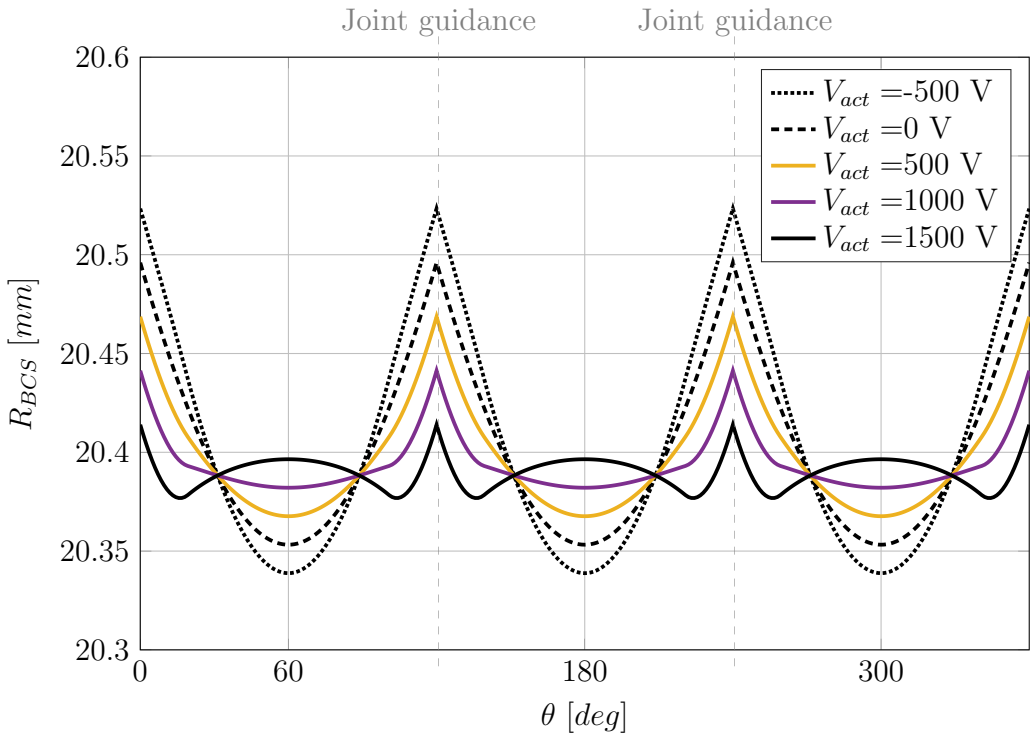

Figure 8. Actuated radius (with respect to the bearing coordinate system) of the AAFB with lightly non-circular shape in unloaded state for different actuation voltage.

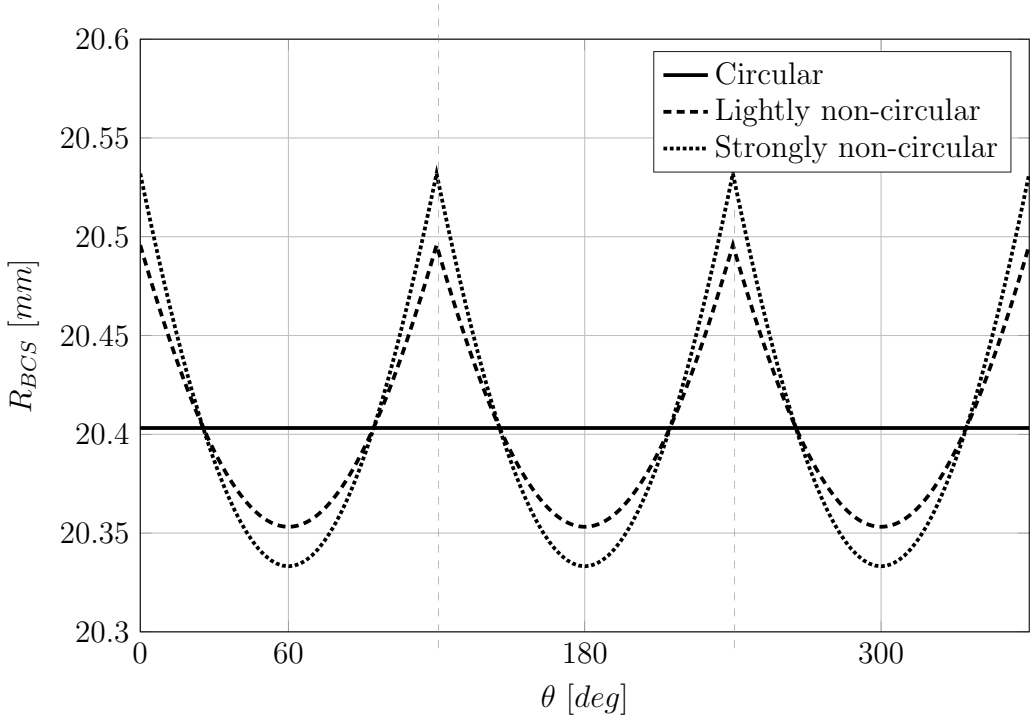

Figure 9. Radius of target shapes during conceptual design of the AAFB [11] (with respect to the bearing coordinate system) .

measure of the deviation between the given and the desired deformation has to be specified. Such a deviation measure maps the given deformation to a simple numeral. Mathematical norms can be applied to the difference between the desired deformation and the deformation achieved during actuation. The H_2-norm is chosen for the evaluation of divergence in this paper taking into account the following mathematical definition:

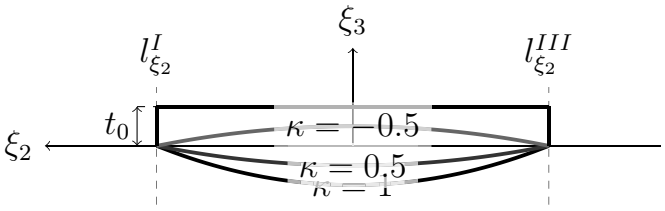

Figure 10. A single supporting shell considering different values for convexity.

$$H_2 = \left(\int_{\theta_s}^{\theta_e} \left(w_{\text{target}}(\theta) - w_{is}(\theta, V_{\text{act}}, \kappa, t_0) \right)^2 \mathrm{d}\theta \right)^{\frac{1}{2}} \tag{29}$$

For an optimal approximation, the formulated norm must reach the possible minimum value. Since the determination of a minimum is an extreme value problem, the norm function must be differentiable with respect to the optimization variables for the entire scope of investigation. In the calculation of the ideal shape, external loads were neglected. By considering only linear expansion terms, the calculation effort is further minimized without causing significant losses in calculation accuracy. The shape optimization starts with the calculation of the deformation w_{is} depending on the operating voltage V_{act} for a given parameter set. The error between the intended deformation w_{target} and the actual deformation w_{is} is then calculated using the H_2-norm from equation (29). This deviation error is still dependent on the control voltage. The algorithm then continues searching for the control voltage where the error is minimal. It should be noted that the control voltage must be limited to the input signals applicable by the used actuator. If the control voltage determined in this way is used in the printout for the calculation of deviation, the minimum error for the given parameter set results from shell thickness and convexity. Repeating this process results in an optimization surface that reflects the relationship between the deviation error and the optimization parameters. Within this optimization range it is now possible to search for the parameter set with the smallest error, i.e. the best match between w_{is} and w_{target}.

5.1.3. Optimization results. The optimization results regarding the AAFB with initially circular and goal-oriented, lightly non-circular configurations are shown in figure 11. With a small shell thickness, the deformation tends to be greater, so that the error between the actual deformation and the nominal deformation is smaller, but no optimum shape control can be achieved. Therefore, the optimization algorithm tries as far as possible to achieve a configuration close to the target shape that leads to the actuation with minimum voltage allowed by the MFCs (−500 V). The most important step towards shape optimization for the discussed goal is therefore to increase the deformation of the bearing shells. To achieve this, the shells must be bent open, which requires contraction of the actuators for which the MFC actuators used require a higher negative voltage signal. The piezoelectric effect, however, limits the operating voltage in the negative range with respect to repolarization effects (and in the positive range by the breakdown

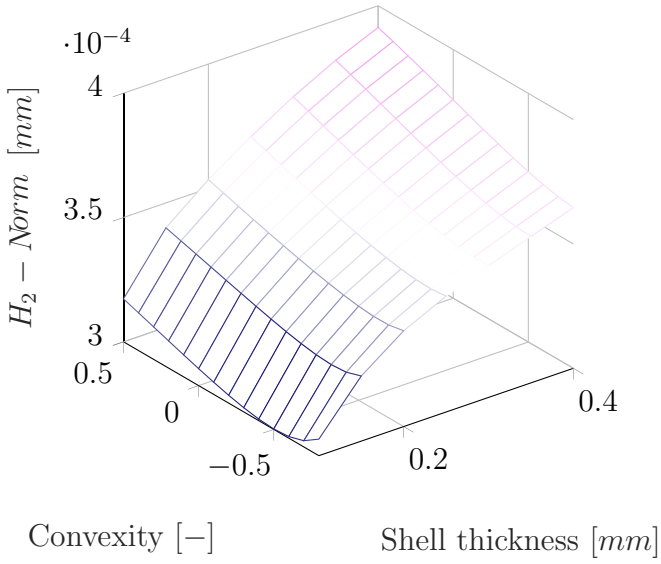

Figure 11. Optimization surface for shape adaptation from circular to lightly-preloaded AAFB with.

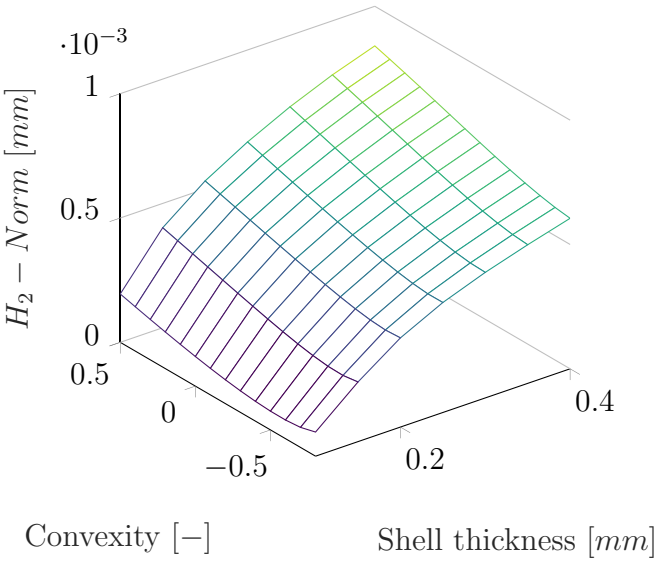

Figure 12. Optimization surface for shape adaptation from lightly-preloaded to circular AAFB with regard to convexity and thickness.

voltage), which should be avoided. Alternatively, d_{31} actuators can be used for the circular configuration as this solution would allow the actuators to operate in a wider range of positive control voltages.

Another promising approach is to make better use of the operating range of the piezo actuators already in use by manufacturing the bearing shells in the non-circular state. They would then be deformed back into a circular shape by means of a positive voltage signal. In the positive voltage range, the control limit is 1500 V , so the triple voltage range can be used. In line with this, figure 12 depicts the optimization surface and required voltage for an optimal shape change from

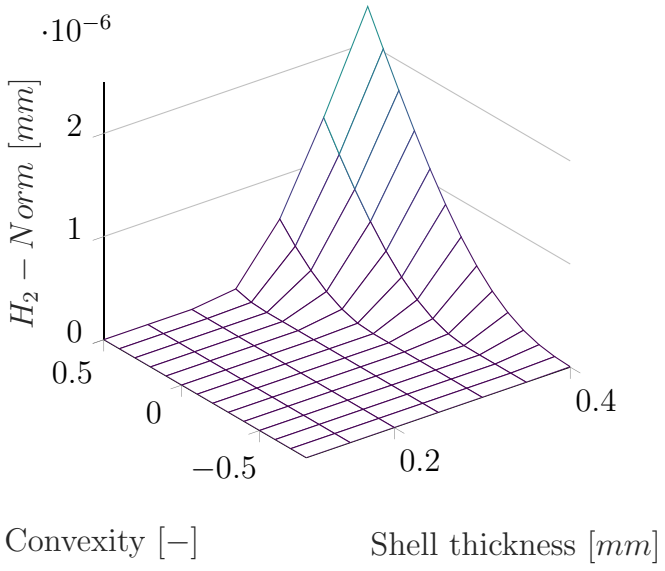

Figure 13. Optimization surface for shape adaptation from lightly-preloaded to strongly-preloaded AAFB with regard to convexity and thickness.

Table 2. Bump-foil parameters for the simulation.

Parameter	Value
Foil thickness	0.101 [mm]
Bump half length	1.778 [mm]
Bump height	0.508 [mm]
Bump pitch	4.57 [mm]
Number of bumps	9 [1/Pad]
Young's modulus	213 [GPa]
Poissons ratio	0.29 [-]

lightly-preloaded to circular target configuration. It is an interesting observation, that the shape adaptation from a lightly-preloaded configuration to circular form is more accurate for a shell thickness below 0.2 mm and inaccurate for a thicker supporting shell compared to the shape control in opposite direction. This observation shows that depending on how local stiffness (or mass and damping in dynamic case) is distributed, the applied work on the structure by piezoelectric patches results into an entirely different actual shapes (in this case a deteriorated shape control for thicker shells).

A further optimization analysis is performed on the lightly preloaded configuration with regard to the strongly preloaded configuration as the target form. The results of this study are shown in figure 13. As can be seen, in this case a perfect shape adaptation is possible for each convexity and for the thickness equal to and smaller than 0.25 mm (thicker than 0.1 mm). As the thickness increases, the convexity must be reduced in order to adapt the bearing shells optimally to the strongly preloaded shape. When calculating the ideal shape in this study, external loads are neglected. However, a similar analysis can be carried out for a specific scope of application, taking into account the loads occurring in the entire operating range.

5.2. Results of AAFB performance in operation

The iterative calculation method for an operative state is schematically shown in [11]. In detail, the calculation tool starts from the assumption of a predefined eccentric position of the journal and begins with the calculation of the hydrodynamic pressure, taking into account the undistorted clearance. The static behavior of the AFBs under a given load and at any speed can be simulated by the iterative solution of the Reynolds differential equation derived at the bearing plane with θ and Z as circumferential and dimensionless axial coordinates, compressible gas flow assumption for an ideal gas, as follows:

$$\frac{\partial}{\partial\theta}\left(P_0{H_0}^3\frac{\partial P_0}{\partial\theta}\right)+\frac{\partial}{\partial Z}\left(P_0{H_0}^3\frac{\partial P_0}{\partial Z}\right)=\Lambda\frac{\partial}{\partial\theta}\left(P_0H_0\right) \tag{30}$$

in contraction with the film thickness function:

$$H_0=h_0/c_0=C(\theta,P_0)+\epsilon\cos(\theta-\gamma)+U_0 \tag{31}$$

where $P_0(=\frac{p_0}{p_a})$ is the dimensionless static pressure, H_0 is the static dimensionless gas film thickness and Λ is the dimensionless rotational speed also known as bearing or compressibility number. Moreover, $C(\theta,P_0)$ is the profile of radial clearance (for the centric position of the journal) from equation (25) in a non-dimensional form, which is mainly focused in current work to be actively adjusted by suggesting an adaptive strategy. It should be noted that the bearing radial clearance in an AAFB also changes due to the load conditions related to the hydrodynamic pressure in the air foil bearing as the main system, as the rigid bearing housing is replaced by an adaptive mechanism to actuate the bearing inner contour. In addition, ε is the non-dimensional eccentricity of the journal with respect to bearing in-plane coordinates and U_0 is the normalized deflection of the foil structure under the static pressure load in radial direction (modeled according to the NDOF approach [26]). In addition, p_a is the ambient pressure used to represent the equation (30) in dimensionless format. Further details of the physics behind AFBs are not the main topic of this paper (see [11]) and the focus is on the adaptive interface of the AAFB. The same three-pad AAFB investigated in [11] using measured stiffness coefficients is considered during the investigation in this section. Initial design parameter of the AAFB with 40 mm bearing length and 38 mm diameter (in circular configuration) are listed in table 2. The model introduced in previous sections considering the flexure joints with calculated stiffness matrix is used here in order to calculate the deformation of three segments of the preloaded AAFB to consider the actual clearance. Accordingly, an additional loop is added to the calculation code to update the clearance under the influence of reaction forces of the bump strip on the supporting shells extracted from the NDOF model. It is assumed that the bearing shells are in a lightly non-circular configuration (with $r_p = 285\ \mu$m and $c_0 = 335\ \mu$m) in the non-activated state ($V_{\text{act}} = 0$ V). Figure 14 shows the change in bearing non-circularity of preloaded AAFB with adaptable supporting shells at 20 krpm under 5 N static load (half the rotor weight) after convergence has been achieved. Based on

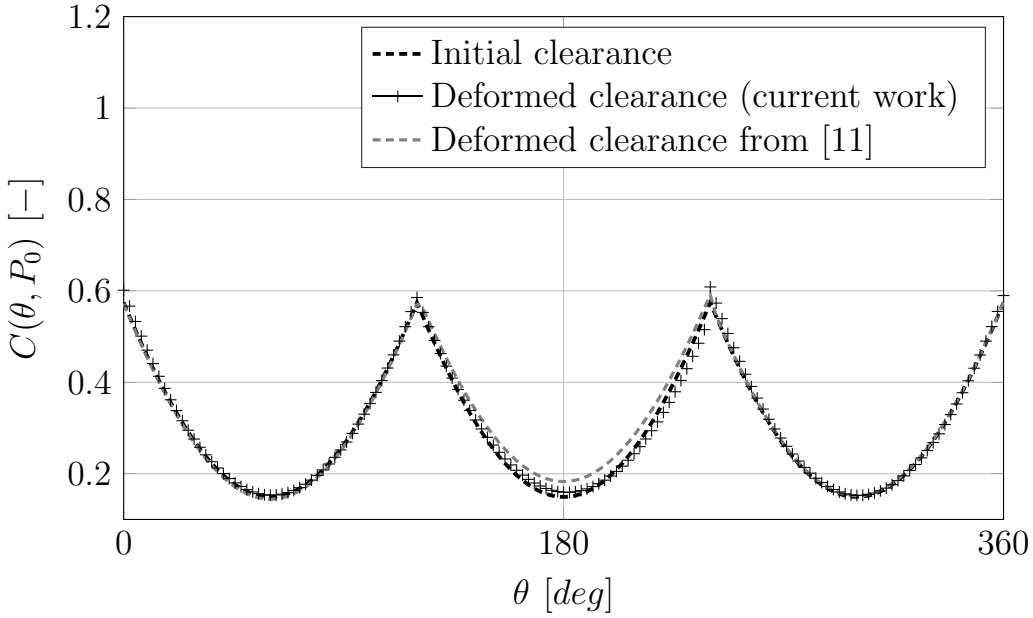

Figure 14. Initial and deformed clearance of AAFB with preloaded configuration, $\omega = 20$ krpm.

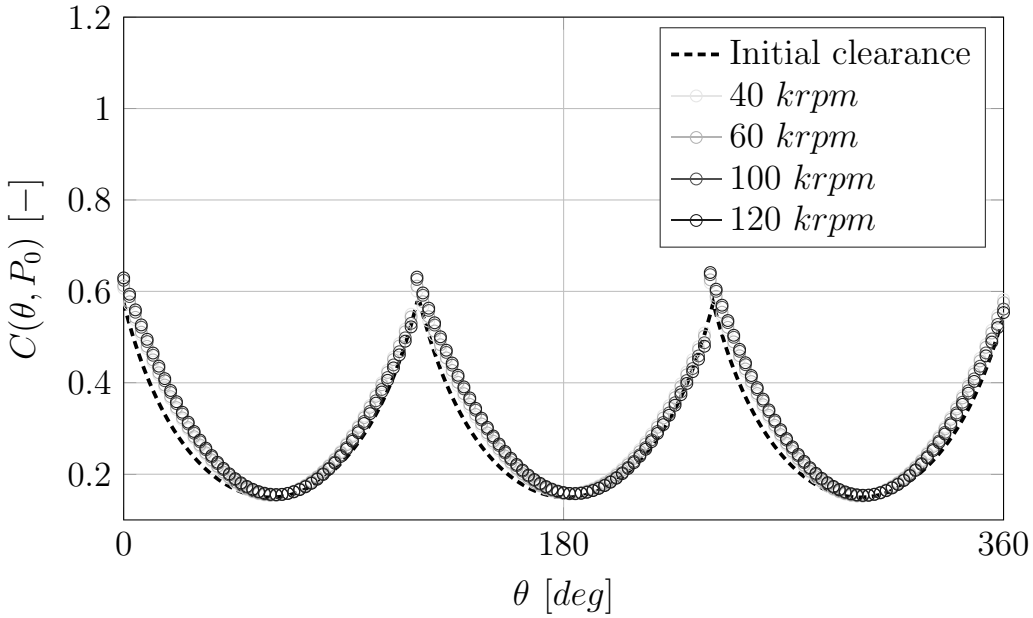

Figure 15. Initial and deformed clearance of AAFB with preloaded configuration, $\omega = 120$ krpm.

the observations from both models, the preload effect of the predominantly loaded bearing shell is reduced in relation to the effective pressure profile built-up. However, this effect is significantly lower for the results from the model presented in this chapter compared to the rigid-body model. In contrast, the tilting effect simulated by the current model is the dominant type of deformation that occurs with the bearing shells in operation. In detail, in this model the external work is largely applied for deformation in bearing shells. In contrast, when using the model presented in this paper, a larger amount of electrical energy, converted by actuators into strain energy, is directed to the joints, since the joints are modeled with a stiffness matrix of 6×6, resulting in a larger tilting effect and less deformation of the shells. For further investigations figure 15 shows the initial and deformed clearance for a higher rotational speed. The tilting effect at higher operating speeds is increased in view of the stiffening effect occurring in the air film, which leads to increased reaction forces during deformation of the bearing shells in an area where the main shell supports the active bumps.

6. Conclusion

A semi-analytical model is developed and discussed in this study to estimate the AAFB performance considering the adaptive interface. The presented model benefits from weighted residual approaches with a compromise between accuracy and computing time to mathematically consider the physical analysis of the adaptive shells. The comparison of simulated results on the actuated deformation of the functional model with experimental observations from previous studies ca n be regarded as proof for the plausibility of assumed approximate basic functions for the specific scope of the investigation. Accordingly, the model presented can efficiently consider the physical behavior of the adaptive interface and further optimize it for practical application with small loads and low-frequency dynamic excitations and other boundary conditions considered in this work. As a remarkable result, it should be noted that the shapes aimed for in conceptual studies of a solution with regard to shape control cannot always be achieved in practice due to physical limitations. With the help of an efficient mathematical model of the adaptive interface, however, it is possible to optimize the various electromechanical parts involved in the concept in order to achieve maximum percentages of the advantages of ideal target shapes. In this context, a method for shape optimization with focus on the functional model is discussed to investigate the ability of the mechanism to efficiently change actuated shapes between different initial and target shapes previously presented in concept studies. This study continues with the variable local stiffness of the bearing shells by locally changing the thickness, as an example of shape optimization. The shell thickness and convexity are then used as optimization variables that are set for optimal shape control between the target shapes. The results of the AAFB operational simulation show that the dynamic and static operating conditions can influence the design objectives of the shape morphing vice versa. These effects need to be accurately identified, taking into account not only the nominal shape of the mechanism but also the efficiency of the solution for loaded operating conditions.

Nomenclature

c_0	Nominal radial clearance	m
$[C_J]$	Stiffness matrix of flexure joints	-
$[C_{p,np}]$	Stiffness matrix	-
$[d_p]$	Matrix of piezoelectric strain constants	$\frac{pC}{N}$
$\{D_p\}$	Vector of electrical charge displacement	$\frac{C}{m^2}$
$[e_p]$	Matrix of direct piezoelectric coefficients	$\frac{N}{Vm}$
$\{E_p\}$	Vector of electrical field strength	$\frac{V}{m}$
f^i_{reac}	Reaction forces of bump foil	Nth
h_0	Gas film thickness in steady-state condition (**LC**)	m
K_{ξ_1,ξ_2}	Shear correction factor	-
p_0	Pressure in steady-state condition (**LC**)	Pa
r	Journal radius	m
$R_{0\ \mathrm{V}}$	Shell radius before actuation (**LCS**)	m
$\Delta R_{0\ \mathrm{V}}$	Change of shell radius with respect to $R_{0\ \mathrm{V}}$ (**LCS**)	m
R_0^{BCS}	Shell radius before actuation (**BCS**)	m
$R_{\mathrm{act}}^{\mathrm{BCS}}$	Actual shell radius after actuation (**BCS**)	m
$R_{\mathrm{target}}^{\mathrm{BCS}}$	Target shell radius (**BCS**)	m
r_p	Preload	m
$[S_p]$	Compliance matrix of piezoelectric materials	$\frac{m^2}{N}$
T	Kinetic energy	Jth
t_s	Shell thickness	m
u_{ξ_1,ξ_2,ξ_3}	Displacement terms of bearing shell with respect to local coordinate system	m
U_s	Displacement vector of bearing shell with respect to local coordinate system	m
V_{act}	Actuation voltage	V
W_{ex}	External work	Jth
ε	Dimensionless eccentricity in steady-state condition (**LC**)	$\frac{e}{c}$
$\{\epsilon_{p,np}\}$	Vector of mechanical strain	-
$[\eta_p]$	Matrix of dielectric constants (Permittivity)	$\frac{C}{Vm}$
θ_p	Pivot angle of the pad or lobe	rad
κ	Convexity factor	-
$\{\sigma_{p,np}\}$	Vector of mechanical stress	$\frac{N}{M^2}$
ω	Rotor angular frequency	$\frac{rad}{s}$
Π	Strain energy	Jth
x, y	Bearing in-plane coordinates	m
z	Bearing coordinate in axial direction	m
θ	Bearing coordinate in circumferential direction	rad
ξ_1, ξ_2, ξ_3	Shell local coordinates in axial, circumferential and radial directions	m

ORCID iDs

Hossein Sadri https://orcid.org/0000-0002-2551-605X
Michael Sinapius https://orcid.org/0000-0002-1873-9140

References

[1] Vasista S, Riemenschneider J, Keimer R, Monner H P, Nolte F and Horst P 2019 Morphing wing droop nose with large deformation: Ground tests and lessons learned *Aerospace* **6** 111

[2] Sinapius M 2018 *Adaptronik* (Berlin: Springer)

[3] Martowicz A, Roemer J, Lubieniecki M, Zywica G and Baginski P 2020 Experimental and numerical study on the thermal control strategy for a gas foil bearing enhanced with thermoelectric modules *Mech. Syst. Signal Process.* **138** 106581

[4] Kim T H and Andres L S 2009 Effects of a mechanical preload on the dynamic force response of gas foil bearings: Measurements and model predictions *Tribol. Trans.* **52** 569–80

[5] Kim D 2007 Parametric studies on static and dynamic performance of air foil bearings with different top foil

geometries and bump stiffness distributions *J. Tribol.* **129** 354
[6] Sim K, Lee Y-B and Kim T H 2013 Effects of mechanical preload and bearing clearance on rotordynamic performance of lobed gas foil bearings for oil-free turbochargers *Tribol. Trans.* **56** 224–35
[7] Sim K, Lee Y-B and Kim T H 2014 Rotordynamic analysis of an oil-free turbocharger supported on lobed gas foil bearings predictions versus test data *Tribol. Trans.* **57** 1086–95
[8] Chasalevris A and Dohnal F 2016 Enhancing stability of industrial turbines using adjustable partial arc bearings *J. Phys. Conf. Series* **744** 012152
[9] Park J and Sim K 2018 A feasibility study of controllable gas foil bearings with piezoelectric materials via rotordynamic model predictions *ASME Turbo Expo 2018: Maintenance, Repair and Overhaul in the Light of Digitalization* June 11-15,2018, Oslo, Norway
[10] Guan H, Liu T, Zhang T, Feng K and Guo Z 2018 Vibration control for rotor mounted on a novel active bump type foil bearing with controllable mechanical preloads *ASME Turbo Expo 2018: Maintenance, Repair and Overhaul in the Light of Digitalization* June 11- 15,2018, Oslo, Norway
[11] Sadri H, Schlums H and Sinapius M 2019 Investigation of structural conformity in a three-pad adaptive air foil bearing with regard to active control of radial clearance *J. Tribol.* **141** 081701
[12] Sadri H 2018 A semi-analytical model of shape-control in an adaptive AIR foil bearing *Proc. of the ASME 2018th Conf. on Smart Materials Adaptive Structures and Intelligent Systems*
[13] Kassegne S K and Reddy J N 1998 Local behavior of discretely stiffened composite plates and cylindrical shells *Compos. Struct.* **41** 13–26
[14] Cheng J, Wang B and Shan-Yi D 2005 A theoretical analysis of piezoelectric/composite anisotropic laminate with larger-amplitude deflection effect, part i: Fundamental equations *Int. J. Solids Struct.* **42** 6166–80
[15] Cheng J, Wang B and Shan-Yi D 2005 A theoretical analysis of piezoelectric/composite laminate with larger-amplitude deflection effect, part ii: Hermite differential quadrature method and application *Int. J. Solids Struct.* **42** 6181–201
[16] Hadjigeorgiou E P, Stavroulakis G E and Massalas C V 2006 Shape control and damage identification of beams using piezoelectric actuation and genetic optimization *Int. J. Eng. Sci.* **44** 209–421
[17] Koconis D B, Kollar L P and Springer G S 1994 Shape control of composite plates and shells with embedded actuators i. voltages spezified *J. Compos. Mater.* **28** 415–58
[18] Shivakumar J and Ray M C 2007 Geometrically nonlinear analysis of antisymmetric angle-ply smart composite plates integrated with a layer of piezoelectric fiber reinforced composite *Smart Mater. Struct.* **16** 754–62
[19] Agrawal B N, Adnan Elshafei M and Song G 1997 Adaptive antenna shape control using piezoelectric actuators *Acta Astronaut.* **40** 821–6
[20] Lim C W and He L H 2004 Three-dimensional exact solutions for the electromechanical response of triple-layer piezoelectric actuators *Smart Mater. Struct.* **13** 1050–8
[21] Lim C W, Cheng Z-Q and Reddy J N 2006 Natural frequencies of laminated piezoelectric plates with internal electrodes *ZAMM* **86** 410–20
[22] Reddy J N and i i u C F 1987 A higher-order theory for geometrically nonlinear analysis of composite laminates *NASA Contractor Report 4056*
[23] Riemer M 1993 *Mathematische Methoden der Technischen Mechanik* 2nd edn (Berlin: Springer)
[24] Gross D 2014 *Technische Mechanik* (Berlin: Springer)
[25] (https://www.smart-material.com/media/Datasheets/MFC_V2.3-Web-full-brochure.pdf) 2019
[26] Le Lez S, Arghir M and Frene J 2007 A new bump-type foil bearing structure analytical model *J. Eng. Gas Turbines Power* **129** 1047